Available online at www.sciencedirect.com

ScienceDirect

journal homepage: www.elsevier.com/locate/he

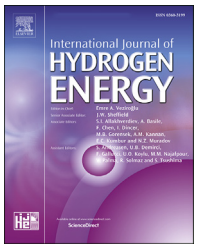

Direct measurement and modeling relative gas diffusivity of PEMFC catalyst layers: The effect of ionomer to carbon ratio, operating temperature, porosity, and pore size distribution

Sina Salari [a], *Jürgen Stumper* [b], *Majid Bahrami* [a,*]

[a] *Laboratory for Alternative Energy Conversion (LAEC), School of Mechatronic Systems Engineering, Simon Fraser University, 250-13450 102 Avenue, Surrey, BC, V3T 0A3, Canada*

[b] *Automotive Fuel Cell Cooperation Corporation, 9000 Glenlyon Pkwy, Burnaby, BC, V5J 5J8, Canada*

ARTICLE INFO

Article history:
Received 30 April 2018
Received in revised form
28 June 2018
Accepted 5 July 2018
Available online 30 July 2018

Keywords:
Catalyst layer
Gas diffusivity
Modified Loschmidt cell
Ionomer to carbon ratio
Ionomer coverage
Operating temperature

ABSTRACT

A modified Loschmidt cell was used to measure the relative gas diffusivity (D^*) of the porous catalyst layers (CLs) of polymer electrolyte membrane fuel cells as a function of CL ionomer/carbon weight ratio (I/C) (0.5, 1.1, and 1.5) and operating temperature (20, 40, and 72 °C). D^* decreased by 80% when I/C was increased from 0.5 to 1.5. While the effective gas diffusivity of CL increased with temperature, D^* decreased because binary diffusion increases more rapidly than Knudsen diffusivity with temperature. The structure of CL was modeled through considering a packed-sphere model for carbon particles within agglomerates, and a network of overlapped spherical agglomerates forming the CL. The gas diffusion problem was solved analytically for the CL structure considering both Knudsen and molecular mechanisms, and, results were validated. Using the model, the effect of porosity, pore size distribution and ionomer coverage on gas diffusivity was evaluated.

Introduction

To predict polymer electrolyte membrane fuel cells (PEMFCs) performance several highly coupled governing equations including gas diffusion, thermal diffusion and convection, electrical current, ion, water and water vapor transports should be solved [1]. The change of transport properties of the membrane electrolyte assembly (MEA) components due to the variation of design parameters or operating conditions makes the problem more complicated. Therefore, accurate analytical models for each transport property significantly help to enable the practical use of performance prediction models to optimize MEA design parameters. The catalyst layer (CL) of MEA is a multi-component, agglomerate-type structure layer that makes developing a comprehensive microstructural model a challenging task. An insufficient supply of oxygen to the CL is a limiting factor to achieve high current densities, and therefore, it is vital to improve the oxygen diffusion rate

* *Corresponding author.*
E-mail address: mbahrami@sfu.ca (M. Bahrami).
https://doi.org/10.1016/j.ijhydene.2018.07.035

Nomenclature

A	Area (m^2)
a	Cell dimension (m)
D	Diffusivity ($m^2\ s^{-1}$)
D^*	Relative diffusivity
d	Diameter (m)
l	Effective length (m)
M	Molecular weight ($kg\ mol^{-1}$)
R	Gas diffusion resistance ($s\ m^{-3}$)
r	Radius (m)
T	Temperature (K)
t	Thickness (m)
V	Volume (m^3)

Subscripts

C	Carbon
e	Elemental
eff	Effective
p	Probe
s	Sample
sp	Secondary pore
tot	Total
v	Volume

Greek symbols

ε	Porosity
θ	Angle in circular coordinate system (rad)
λ	Volume loading (m)
ξ	Overlap parameter
φ	Overlap angle (rad)
ρ	Density (kg/m^3)
ν	Volume ratio

within CL [2]. This can be done through experimental and theoretical investigation of CL gas diffusion. While modeling methods such as reconstructing the geometry of CL based on images obtained by focused ion beam scan electron microscopy (FIB-SEM) and nano X-Ray computed tomography (CT[1]) [16–18], or stochastic modeling [19–21] are extremely helpful to understand the transport mechanisms in CL, their complexity halt their use in performance prediction models. On the other hand, available simple analytical models, e.g. effective medium theory [3,4] or percolation theory [5] based models, are convenient to be integrated into the performance prediction models. However, these models use the CL porosity as the only input that highly limits their accuracy considering the fact that changing production parameters, different CLs can be produced (as in Ref. [6]) with the same gas diffusivity values but different porosities (further discussion on shortcoming of gas diffusivity models considering just porosity can be found in Ref. [2]). Therefore, there is a vital necessity for a user-friendly, inexpensive, and timesaving model for gas diffusivity within CL that can be integrated to the performance prediction models, while somehow consider the effect of CL structure as well.

As for experimental data, the gas diffusivity of CL as a part of the whole fuel cell was measured in-situ in Refs. [7–12]. The accuracy of methods deducing the CL diffusivity (in-situ) indirectly by investigating polarization curves of PEMFC is profoundly influenced by the model relating the impedance of the CL to its gas diffusivity [13]. Other studies determined oxygen diffusivity indirectly by use of ex-situ solid state electrochemistry approach [14–16]. According to Rashapov et al., electrochemistry, demands a thick wet layer (several millimeters) creating experimental challenges that compromise the accuracy [12]. Others investigated the gas diffusivity of the gas diffusion layer (GDL) [17–19] or combined GDL-CL electrode [20]; however, evaluation of gas diffusivity of CL alone remains in demand. Researchers reconstructed the geometry of CL based on images obtained by FIB-SEM and nano X-Ray CT [21–23], or stochastic modeling [24–26], and then modeled the gas diffusivity of CL numerically. Nevertheless, direct gas diffusivity measurements are still vital to validate such studies and ensure accuracy. Yu and Carter [27] measured in-plane diffusivity of CL ex-situ using a Wicke–Kallenbach diffusion cell (WKC[2]) and evaluated the effect of I/C and humidity on CL diffusivity. However, most likely in PEMFC, the gas transports through-plane to get to the reaction sites in CL, and, therefore, studies on through-plane direction are necessary as well. CL does not exist as a standalone layer and needs to be coated on a support substrate. For through-plane gas diffusion measurements, the support substrate should be a porous one letting the gas to pass. Coating the CL onto a porous substrate commonly results in penetration of CL into the porous substrate, which compromises the gas diffusion test results. Moreover, finding a porous support substrate with gas diffusion resistance in the same range as CL (2–10 μm thick porous layer with porosity ≅40–70%) is another challenging task. Inoue et al. [22] used WKC to study through-plane diffusivity of CLs with I/C ratios of 0.4–1.4 and different carbon supports, including Black Pearls, Ketjenblack, and graphitized Ketjenblack (the porosity range was 41%–75%). They reported the relative gas diffusivities (that is the ratio of the effective gas diffusivity and binary diffusivity) ranging from 0.01 (for CL with porosity = 41%) to 0.2 (for CL with porosity = 75%). They sprayed the catalyst, and there was no mention of the support substrate. Their CLs were 22–50 μm thick to have a detectible through-plane gas diffusion resistance. Shen et al. [28] also measured through-plane gas diffusivity of sprayed coated CLs on the alumina substrate, with thicknesses ranging from 6 to 29 μm to eliminate the effect of interfacial resistance due to CL penetration into the porous substrate. They used a modified Loschmidt cell (MLC[3]) apparatus and reported the effective gas diffusivity of CL = 0.0015 $cm^{-2}s^{-1}$.

The support substrate, coating method, CL thickness, and processing parameters could affect the CL structure, and, as a result, its gas diffusivity. Therefore, in this study, the production process of CL was explicitly designed to be similar to the one used for PEMFCs. The catalyst samples were prepared using Mayer bar coating with the same thickness and Pt loadings as CLs of fuel cells. The support

[1] Computed tomography.

[2] Wicke–Kallenbach diffusion cell.

[3] Modified Loschmidt cell.

substrate was chosen in a way to obtain uniform CL with minimal penetration of CL into the substrate (in PEMFCs CL is coated or transferred onto the membrane which is a non-porous substrate with almost no penetration of CL into the membrane). CL samples prepared with different I/Cs and the through-plane diffusivities were measured with an MLC testbed at different operating temperatures resembling the operating temperature of PEMFCs. An analytical model was developed for the gas diffusivity that requires I/C and salient geometrical parameters of CL including pore size distribution (PSD[4]) and porosity. The model predicted gas diffusivity values with less than 16% difference from experimental values. Based on the model the effect of porosity and PSD were evaluated on the gas diffusivity of CL and of carbon agglomerates within CL.

Experiment

CL preparation

The catalyst ink was prepared using catalyst powder consisting of Pt nanoparticles deposited on 10–50 nm partially graphitized carbon particles (50% weight, carbon particle mean diameter equal to 30 nm). To prepare the catalyst ink, the powder was dispersed in the solvent which was deionized water and alcohol. Then aqueous ionomer dispersion (Aquivion® PFSA, Solvay) was added. Finally, the ink was placed in a ceramic jar (US Stoneware, model 755 RMW) containing zirconia balls and jar milled for a specific duration. Following previous study [29], CL was coated with Mayer bar on the porous PTFE filters (Fluoropore FHUP04700, EMD Millipore), with 85% porosity and thickness of 50 μm. The substrate was chosen with specific surface property (highly hydrophobic) and pore size (<500 nm) to minimize CL penetration. SEM imaging of CL cross-sections showed two distinct layers (CL and the filter) with no observable catalyst penetration into the filter PTFE (Fig. 1). The uniformity of the CL is also apparent in the image.

To test I/C effect on diffusivity, CL samples with three I/Cs 0.5, 1.1, and 1.5 were prepared. For each design (I/C) at least ten samples were prepared with Pt loadings ranging from 150 μg/cm^2 to 300 μg/cm^2.

CL thickness, porosity, and pore size distribution

The thicknesses of CL samples were measured using SEM images of CL coated substrates cross-sectioned by a freeze-fracture procedure. The CL samples were sandwiched between graphite plates in a sample holder, immersed in liquid nitrogen, and cut at low temperature with a sharp scalpel to yield a cross-section with minimal damage. The thickness of the CL was measured from SEM images taken at three or more locations on each cross-sectioned sample.

The CL porosity was calculated based on the measured thickness, and Pt loadings through Eq. (1):

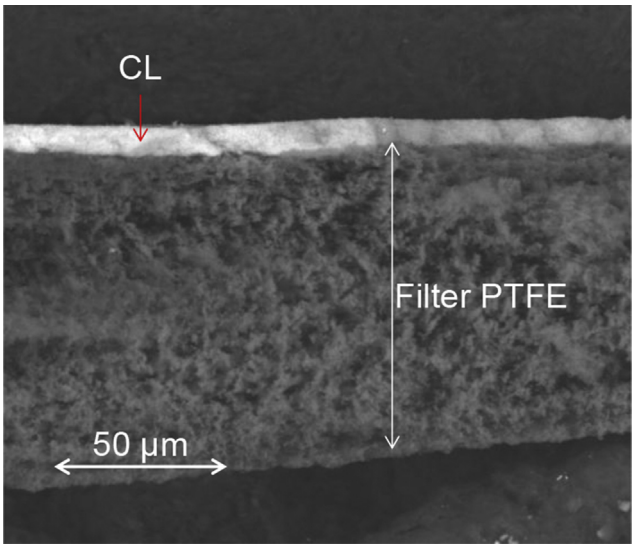

Fig. 1 – SEM image of the cross-section of CL coated with Mayer bar on a filter PTFE substrate. The CL is uniform and there is low catalyst penetration into the substrate.

$$\varepsilon = 1 - (\lambda_{Pt}/\lambda_{CL})\left(\frac{1}{\rho_{Pt}} + \omega_{C/Pt}\left(\frac{1}{\rho_C} + \omega_{I/C}\frac{1}{\rho_I}\right)\right) \quad (1)$$

where λ_{Pt} is the measured platinum loading (kg/m^2), $\omega_{C/Pt}$ is the carbon to platinum weight ratio, $\omega_{I/C}$ is the ionomer to carbon weight ratio, and t_{CL} is the CL thickness (m). The used density values were $\rho_{Pt} = 21.45$ g/cm^3 for Pt [30], $\rho_C = 2$ g/cm^3 for carbon black particles [31], and $\rho_I = 1.9$ g/cm^3 for ionomer [32].

There are different methods to measure the PSD of CL including mercury intrusion porosimetry, SEM imaging techniques, and N_2 adsorption porosimetry. In a previous work [33] all these methods were evaluated for different designs of CL, and one of the comparisons (for CL with I/C = 0.9 and 24 h of catalyst powder milling) is presented in supplementary material for this paper. Although the uncertainty of the PSD obtained by N_2 adsorption applying the classical theory Barrett-Joyner-Halenda (BJH) is related to $[\ln^{-1}(p/p_o)]$, that means for pores larger than 50 nm the uncertainty is high [34], in comparison with other methods, BJH showed promising results. Therefore, N_2 adsorption porosimetry was used to measure CL PSD. A volumetric nitrogen physisorption porosimeter (Autosorb iQ-MP, Quantachrome Instruments) was used to measure the isotherms of CL samples. CL coated on Nafion membrane samples were dried under vacuum for about 10 h at 50 °C. A 9 mm sample cell with bulb and filler rod was loaded with at least 300 mg of catalyst coated membrane for each test. A total of 100–200 data points were collected for each isotherm, and each test was repeated at least three times.

Gas diffusion measurement testbed: modified Loschmidt cell (MLC)

The Loschmidt cell (LC) method is a well-known technique for measuring the binary diffusion of two gases [35]. The LC method is based on a 1D diffusion problem. There are two large gas-filled chambers at the same pressure connected by a

[4] Pore size distribution.

closed valve. At time zero each chamber contains one type of gas, and then opening the valve, the gases diffuse into each other, and the concentration of each one changes with respect to time at any specific location. The analytical solution for this 1-D diffusion problem is explained in Ref. [28]. Comparing the monitored concentrations with the analytical solution the binary diffusivity coefficient is determined. The modified Loschmidt cell (MLC) method also works on the same basis; however, instead of connecting the chambers directly, a porous sample would be mounted between the chambers and the gases have to path through the porous sample from one chamber to the other.

In MLC testbed of this study (Waterloo Technical Instrument Inc. testbed was modified in-house), a sliding gate with slots for porous samples was mounted between the chambers (Fig. 2a). The gate acted as both the sample holder and the valve when the chambers were clamped to the stage (Fig. 2a). The measurement procedure for CL consisted of the following steps:

1. Purge I: At the beginning of the test, the metal part of the stage was between the chambers, isolating them from each other. The upper and lower chambers were flushed with nitrogen and oxygen, respectively.
2. Test I: The stage rotated to a sample slot with a stack of filter PTFEs, allowing the gases to diffuse into the stack and then to the opposite chamber, while the oxygen concentration was monitored over time in a specific location in the nitrogen channel.
3. Purge II: The stage isolated the chambers again to flush and fill each of them with pure nitrogen or oxygen.
4. Test II: The sample holder rotated to the slot with the stack of catalyst coated filter PTFEs, allowing the gases to diffuse into the stack and then to the opposite chamber, while the oxygen concentration was monitored over time in a specific location in the nitrogen channel.

For each test, the oxygen concentration versus time plots for oxygen probe locations were stored. Using a MATLAB code the gas diffusion resistance between the probe in the nitrogen chamber, and the top of the other chamber was calculated, comparing the monitored concentrations with the analytical solution (the detailed theoretical explanation of the code can be found in Ref. [36]). The code changed the resistance value between the chamber boundary and the probe location in the analytical solution till the obtained analytical oxygen concentration vs time curve became the same as the obtained experimental one (or the difference became minimum). Considering Fig. 2b, the relation between the diffusion resistances in the two tests is as follows:

$$R_{II} - R_I = \left(R_{gap\ 2} + \sum_n R_{Filter} + \sum_n R_{CL}\right) - \left(R_{gap\ 1} + \sum_n R_{Filter}\right) = \left(R_{gap\ 2} - R_{gap\ 1}\right) + \sum_n R_{CL} \quad (2)$$

where R_I and R_{II} are the total gas diffusion resistances between the oxygen probe and the top of the oxygen chamber in the tests I and II, respectively; $R_{gap\ 1}$ and $R_{gap\ 2}$ are the resistances of the gas gap in tests I and II, respectively; n is the number of samples per stack in the nitrogen chamber, R_{filter} is the Filter PTFE gas diffusion resistance, and R_{CL} is the CL gas diffusion resistance.

The effective diffusion length of a medium is the length of an equivalent gas filled open space that has the same diffusion resistance as the medium. In terms of effective lengths (l_I and l_{II}), Eq. (2) can be rewritten as follows:

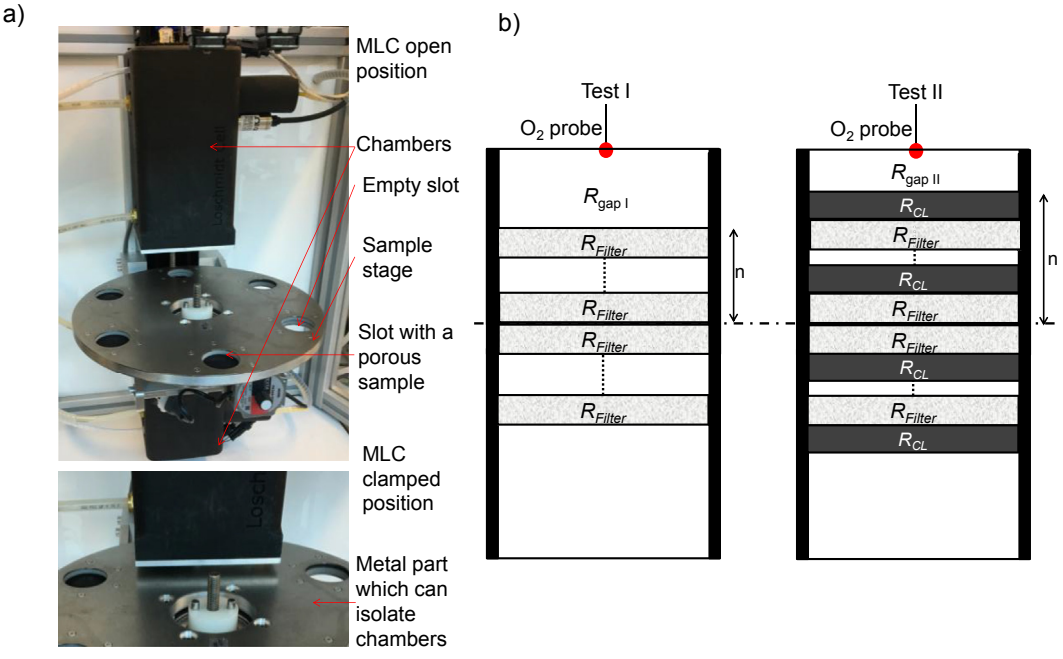

Fig. 2 – a) Modified Loschmidt cell testbed open and clamped positions. b) Test I and II done in MLC to measure CL gas diffusion resistance.

$$\frac{l_{II}}{D_{binary}A} - \frac{l_I}{D_{binary}A} = -\frac{t_{CL\_tot}}{D_{binary}A} + \frac{t_{CL\_tot}}{D_{eff}A} \quad (3)$$

where t_{CL_tot} is the summation of CL samples thickness in the nitrogen channel, D_{binary} is the binary diffusion coefficient for oxygen and nitrogen pair, and D_{eff} is the CL effective gas diffusivity. The porous sample diffusivity can be calculated from Eq. (4):

$$D_{eff} = \frac{D_{binary}t_{CL\_tot}}{(l_{II} - l_I + t_{CL\_tot})} \quad (4)$$

and Eq. (5) shows relative diffusivity:

$$D^* = D_{eff}/D_{binary} = \frac{t_{CL\_tot}}{(l_{II} - l_I + t_{CL\_tot})} \quad (5)$$

Present model

Model overview

The gas diffusivity of CL was found analytically based on an effective medium model. The inputs of the model are porosity, PSD, I/C of CL, and the sample/gas temperature. A simplified geometry was defined for the CL consisting of a network of overlapping spherical agglomerates and spherical carbon support particles. The gas diffusivity of the geometry was found analytically considering both molecular and Knudsen diffusion mechanisms. It predicts the overall diffusivity of CL accurately, and at the same time is easy to implement, making it an excellent candidate to investigate property-performance correlations related to gas diffusion in the CL.

CL structure

The catalyst layer is a micro/nanocomposite structure of carbon support agglomerates, primary and secondary pores, Pt particles supported on carbon particles and ionomer (See Fig. 3a). To model the gas diffusion analytically, the complex geometry of CL should be simplified. The main assumptions required were:

1. Carbon support particles can be envisioned as porous spheres [37].
2. Carbon support particles, Pt particles mounted on their surface and the gaps between them (primary pores) form spherical agglomerates with overlap.
3. Ionomer covers the agglomerates on the surface. The coverage is not 100%; however, it blocks some of the primary pores inside the agglomerates.
4. The CL structure (scale II modeling) is formed from a network of partially ionomer-covered agglomerates with different diameters. These agglomerate diameters were calculated based on the secondary pores diameters from the input PSD.
5. The gas diffusivity of ionomer, carbon support particles and Pt particles are negligible in comparison to the gas diffusivity of primary and secondary pores inside CL, i.e. gas diffusion happens through the pores of the CL (except for pores inside carbon particles as they are several order of magnitude smaller than the primary and secondary pores).
6. The arrangement of carbon particles inside agglomerates is known.
7. The arrangement of agglomerates in CL is known.

Based on these assumptions, the structure of CL was modeled (see Fig. 3b) in two scales: I) the structure within agglomerates, and II) the structure of the network of agglomerates. The size of agglomerates and carbon support particles were calculated based on the size of secondary and primary pores (PSD input) respectively.

Structural model for scale I: pore geometry within agglomerates

To define the pore geometry within agglomerates three parameters should be specified: pore size, pore shape, and pore connectivity. The size of pores within agglomerates was an input to the model from PSD (pores smaller than 20 nm [38,39] were considered as primary pores). The pore shapes and connectivity were modeled by considering pores as gaps between equally sized solid spheres (carbon particles) with orderly-packing. Spherical carbon particles is shown to be reasonable according to experimental images [40] and is widely adopted [2,41]. For the arrangement, face-centered cubic (FCC[5]) was used (details of FCC arrangement can be found in Ref. [42]). Other arrangements were also tried, however, as FCC porosity (=0.26) was the closest one to the randomly packed spheres porosity [43], this arrangement was chosen.

Structural model for scale II: geometry of the network of agglomerates

To model agglomerates, the concept of spherical porous agglomerates touching without overlap was used in Refs. [5,44–47]. However, compared to reconstructed CL geometry from FIB-SEM images [48], CL structure modeled with spherical agglomerates without overlap have overestimated active surface area and gas diffusivity [48]. Therefore, in this study spherical agglomerates with overlap were considered (schematically shown in Fig. 3b), to produce a realistic, lower active surface area. Ionomer partially covered the agglomerates and blocked portion of the primary pores. The overlapping parameter, ξ, was defined as the ratio of the radius of the agglomerate, r, to the cell dimension, a, or as the angle of overlap, $\varphi = \cos^{-1}(1/\xi)$ (Fig. 3b). The angle of overlap was solely a function of geometry relationships, ionomer to carbon volume ratio, the porosity of CL (input), FCC arrangement (=0.26 [43]), and carbon particles (=0.29 [49]):

$$4.5\xi^2 - 2\xi^3 - 1.5 = 2.7(1-\varepsilon)(1.35 + 0.71\upsilon_{I/C})/(1+\upsilon_{I/C}) \quad (6)$$

Size of the unit cell (a) and radius of agglomerates (r_{agg}) was calculated based on the geometrical relationships, overlap angle, and the size of secondary pores (input).

$$a = r_{sp}\Big/\sqrt{(1-\tan(\varphi)) - (\pi - 4\varphi)\xi^2} \quad (7)$$

$$r_{agg} = \xi r_{sp}\Big/\sqrt{(1-\tan(\varphi)) - (\pi - 4\varphi)\xi^2} \quad (8)$$

[5] Face-centered cubic.

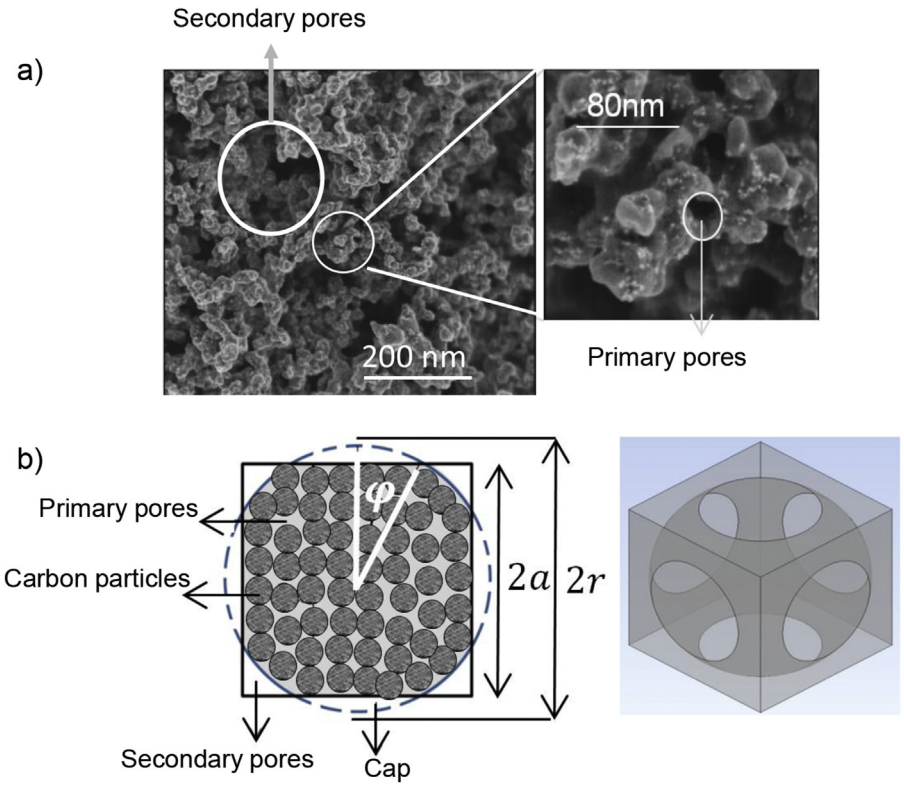

Fig. 3 – a) SEM image of CL which shows the secondary and primary pores within CL. b) Schematic of the unit cell used to model structure of CL.

Primary pores in CL were divided into two groups: the accessible pores that could be reached by gas and the blind pores that gas could not be reached in due to the pores being covered by ionomer. The input porosity to the model was based on theoretical calculations and CL thicknesses calculated by SEM imaging that considered all primary pores, including both blind and accessible ones. The input PSD was determined by N_2 adsorption porosimetry, which only measures accessible primary pores and all secondary pores (as ionomer covered agglomerates on the surface, it was assumed that there were no blind secondary pores). Therefore, the total primary pore volume in the unit cell calculated based on porosity was larger than the primary pore volume in the input PSD (30% vs 3.5% for the CL with I/C = 1.1). Based on this difference, the ionomer coverage was calculated as the ratio of the accessible volume of primary pores (input from PSD) to the volume of all primary pores including accessible and blind pores (calculated from the input porosity).

The thickness of ionomer was calculated based on the volume of ionomer content of CL I/C (input), ionomer coverage, and available surface area of agglomerates (geometry of the unit cell).

The defined unit cell included a pair of the primary and secondary pore. Therefore, all secondary and primary pores from the CL PSD had to be translated into a system of bi-modal pore size distribution including an effective primary pore and an effective secondary pore. As will be explained later, a linear function of diameter was the dominant part of gas diffusivity within primary pores, and therefore, a weighted linear average, based on volume percentage was chosen for the primary pores to calculate the effective primary pore diameter Eq. (9).

$$d_{\text{eff\_primary}} = \frac{\Sigma_i \nu_i \times d_{ppi}}{\Sigma_i \nu_i} \tag{9}$$

where ν_i is the volume ratio of the i^{th} primary pore (pp) in the CL PSD.

In case of the secondary pores, the diffusivity was a complex function of the diameter. As a result, instead of an effective secondary pore, one unit cell was defined for each secondary pore, and the effective property was defined for the diffusivity. The effective diffusivity was calculated through volume-ratio weighted integration over the calculated diffusivity for each pair of the secondary and the effective primary pore Eq. (10).

$$D_{eff} = \frac{\Sigma_j \nu_j \times D_{pair\ j}}{\Sigma_j \nu_j} \tag{10}$$

where D is diffusivity, ν_j is the volume-ratio of j^{th} secondary pore in the PSD. The detailed equations' derivations can be found in Appendix B.

Diffusivity modeling within the agglomerates

The relative diffusivity of agglomerates was calculated considering both molecular and Knudsen mechanisms as follows [50]:

$$D^* = D_{eff}/D_{binary} = \left(D_{binary}/D_{molecular} + D_{binary}/D_{Kn}\right)^{-1} \quad (11)$$

Kn diffusivity was calculated from Eq. (11) [51]:

$$D_{Kn} = (8/3) r_{pore} \sqrt{RT/2\pi M} \quad (12)$$

where R is the gas constant, 8.314 J mol^{-1} K^{-1}, M is the molecular weight of the gas (kg/mol), and r_{pore} is the radius of the pore (m). Primary pores are less than 20 nm [38,39] in diameter and the mean free path of oxygen at room temperature and atmospheric pressure is 63 nm [52]; thus Knudsen diffusion is dominant for primary pores, which is a linear function of pore radius; therefore, an effective primary pore radius based on linear averaging on all primary pores can be used for diffusivity calculations.

In Eq. (11), the Knudsen to binary ratio was calculated through Eq. (12) and literature values for binary diffusion. The molecular to binary diffusion ratio represents the effect of the pore shape and the connectivity of pores in the porous medium in comparison to open space, which is solely a function of geometry shape and not pore size or thermodynamic conditions. Assuming 1D diffusion problem for FCC arrangement, and considering a network of infinitesimal resistances (Fig. 4a), the ratio of molecular gas diffusivity of FCC arrangement to binary diffusion was calculated to be 0.11. In the calculations the diffusion within the carbon particles (solid part of FCC arrangement) assumed to be zero in comparison to the gas diffusion in the pore part (= 1).

The agglomerate diffusivity was calculated by substituting the FCC arrangement diffusivity and Knudsen diffusivity (Eq. (12)) into Eq. (11):

$$D_{agg} = \left(9.09/D_{binary} + 0.37 r_{pore}\sqrt{M/RT}\right)^{-1} \quad (13)$$

Diffusivity within CL

There is no exact analytical solution for gas diffusion within the defined unit cell in the literature as it is a complex geometry. However, assuming a 1-D simplification, a network of infinitesimal series resistances could be used to calculate the relative diffusivity of the unit cell as well (see Fig. 4b). Considering Fig. 4c each element had two parts: agglomerate part which its diffusivity obtained from Eq. (13), and secondary pore part. Eq. (11) was used to calculate the gas diffusivity in the secondary pores (D_{sp}), substituting binary diffusivity for the molecular diffusivity term (ratio = 1) and calculating Kn diffusion term based on the secondary pore diameter (Eq. (12)). Then the overall gas diffusion resistance was obtained integrating the elemental resistances over the entire domain:

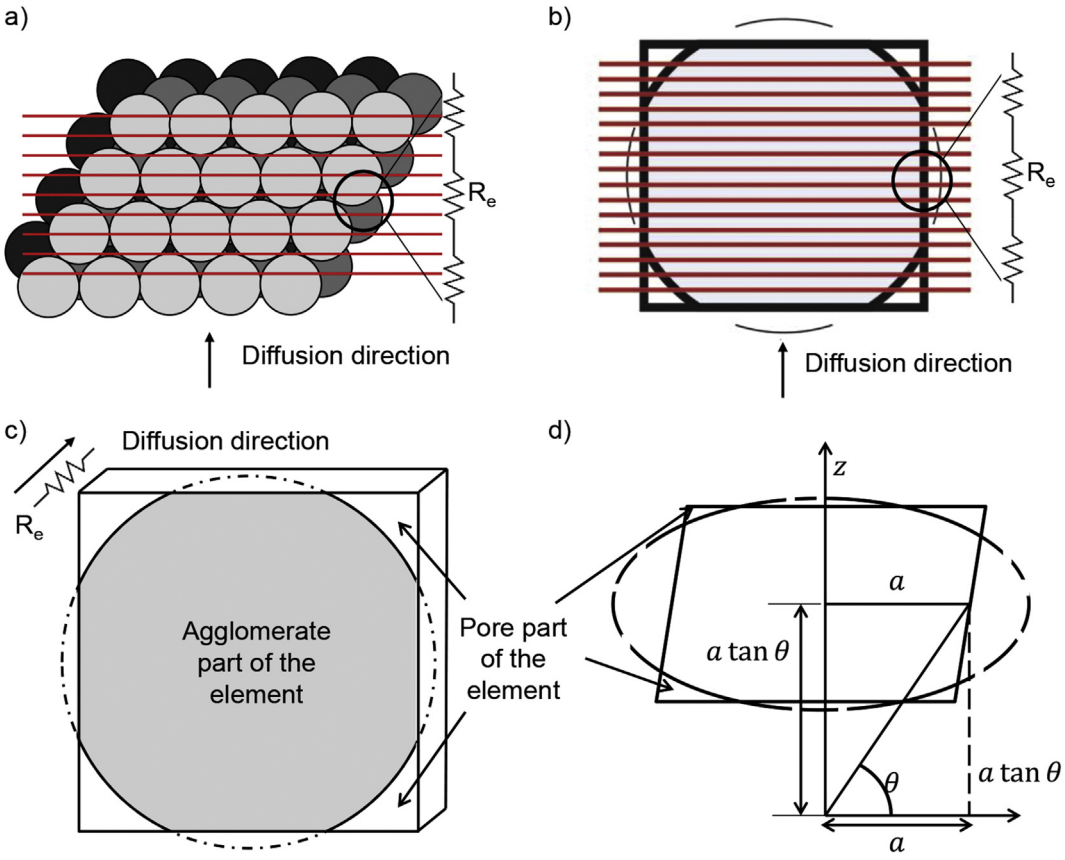

Fig. 4 – The network of series resistances for the a) FCC arrangement, b) Unit cell. The red lines represent the imaginary cross-sections which form the elemental resistances. c) Schematic of the considered diffusion resistance element. d) The geometrical parameters of the gas diffusion resistance element. (For interpretation of the references to color/colour in this figure legend, the reader is referred to the Web version of this article.)

$$R = \frac{2}{aD_{sp}}\left(\int_{0}^{\cos^{-1}\left(\frac{1}{\xi}\right)} \frac{\frac{\left(1+\tan\theta^2\right)}{4}d\theta}{1-\left(1-\frac{D_{agg}}{D_{sp}}\right)\left(\tan(\varphi_e)+\xi_e^2\left(\frac{\pi}{4}-\varphi_e\right)\right)} + \int_{\cos^{-1}\left(\frac{1}{\xi}\right)}^{\frac{\pi}{2}-\cos^{-1}\left(\frac{1}{\xi}\right)} \frac{\xi\cos\theta d\theta}{4-\left(1-\frac{D_{agg}}{D_{sp}}\right)\left(\tan(\varphi_e)+\xi_e^2\left(\frac{\pi}{4}-\varphi_e\right)\right)} \right) \quad (15)$$

where ξ_e and φ_e were elemental overlap parameters calculated form Eqs. (16) and (17) respectively:

$$\xi_e = \sqrt{\xi^2 - tan^2\theta} \quad (16)$$

$$\varphi_e = \cos^{-1}\left(\frac{1}{\xi_e}\right) \quad (17)$$

where θ is the angle shown in Fig. 4d. The detailed equations' derivations can be found in Appendix B.

Results

Thickness, porosity and pore size distribution

The CL thickness measurement and calculated porosities (Eq. (1)) results are given in Table 1, and the measured PSDs are brought in Fig. 5.

The porosity of CL dropped from 69% to 48% for I/C = 0.5 to I/C = 1.5, and the volume of pores greater than 200 nm vanished for I/C = 1.5. As, ionomer mostly fills the secondary pores in CL and does not penetrate into primary pores [53], increasing the ionomer content of CL from 0.5 to 1.5 should reduce both the void space of CL (porosity) and the volume of large secondary pores. While ionomer fills the secondary pores, it also blocks part of primary pores inside the agglomerates by covering the agglomerates. As a result, adding ionomer to the catalyst cut pore volume from both ends and increased the volume percentage of pores in the middle area (20 nm–100 nm).

Relative diffusivity of CL

Fig. 6 shows the measured and modeled relative diffusivity values for CL samples with I/Cs = 0.5, 1.1, and 1.5 at temperatures ranging from 20 to 72 °C. The modeled relative diffusivity values matched the experimental values and the difference was less than 16%. The difference was higher for

Table 1 – CL samples' thicknesses measured by SEM imaging (±measurement standard deviation) and porosities calculated from Eq. (1) (±calculated standard deviation).

	Thickness (μm)	Porosity (%)
I/C = 1.5	9.0 ± 1.0	48 ± 5
I/C = 1.1	7.0 ± 0.8	58 ± 8
I/C = 0.5	9.3 ± 1.3	69 ± 10

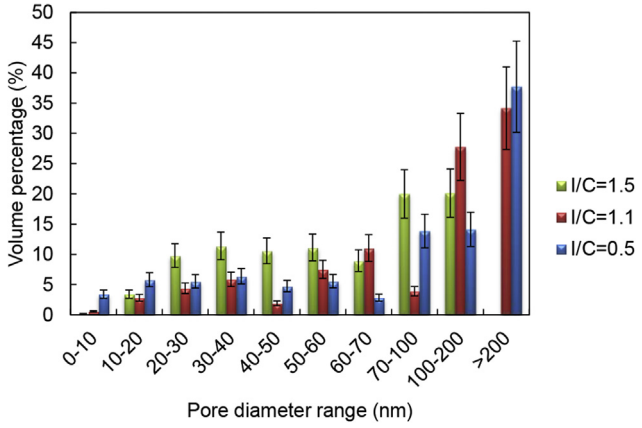

Fig. 5 – Pore size distribution of CL samples with I/C = 0.5, 1.1 and 1.5, measured by N_2 adsorption applying BJH theory. The error bars are standard deviations of measurement repetitions.

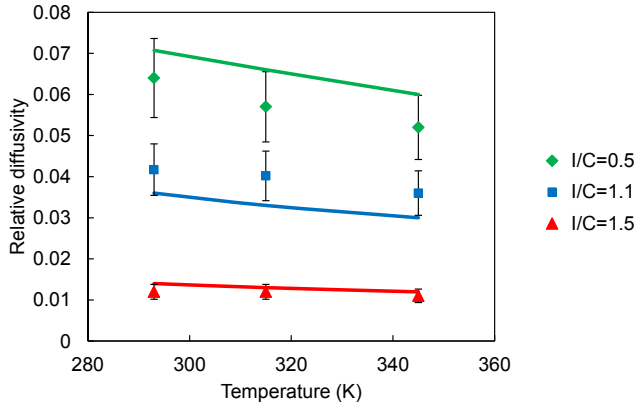

Fig. 6 – Relative diffusivity for CL samples with I/C about 0.5, 1.1, and 1.5, in different temperatures. The error bars shows the standard deviation of at least 10 measurements. The lines indicate the gas diffusivity values calculated using the model.

CLs with lower ionomer contents. To understand the reason, the CL PSDs should be evaluated. As mentioned in section 2.2 of this study, the BJH theory is a qualitative method to measure PSD [34] derived for mesopores (2–50 nm), and the PSD uncertainty is proportional to the pore size. As a result, the measured PSD for designs with high ionomer content was the most accurate one (most of the pores were in the proper pore detection range of BJH method), which led to the most accurate modeled relative diffusivities.

The simplified geometry, and use of Eq. (11) to include Kn diffusion, most likely contributes to the difference between the modeled and experimental relative diffusivities as well. Pant et al. [54] showed using Eq. (11) sometimes led to deviation from experimental results. More accurate models proposed by Pant et al. that demand complicated numerical solutions. To solve the problem analytically use of these models was not considered in this study.

Besides the limited accuracy of input PSD, and the use of Eq. (11) to include Kn diffusion, it should be pointed out that

the model accuracy could be affected also by assuming agglomerate-type porous structures for CLs with disordered agglomerate network, or for CLs containing C–Pt particles far from spherical particles (discussion on carbon particle morphology can be found in Ref. [55]). Also the assumption that ionomer only fills the secondary pores, is not completely valid for CLs with high ionomer content (not enough space between agglomerates).

To further validate the agglomerate size distribution (ASD[6]) calculated by the present model, the porosity and pore size distribution obtained by reconstructing geometry of a X-Ray Nano-CT for a CL in Ref. [56] was used. The resulting ASD was compared to the ASD presented in Ref. [56], and the results were consistent (Available in supplementary material) [57].

The modeled relative diffusivity values without Knudsen effect ($D_{kn} = \infty$) for I/C = 0.5, 1.1, and 1.5 were about 0.41, 0.46, 0.29 respectively independent of the operating temperature, that were about one order of magnitude greater than the experimental values highlighting the importance of considering Knudsen diffusion.

Evaluating diffusivity of CL with different I/Cs

80% decrease in relative diffusivity was observed as the I/C ratio in CL increased from 0.5 to 1.5. Yu and Carter [27] also measured a sharp ~95% decrease in relative diffusivity when comparing CL with I/C = 0.5 to CL with I/C = 1.5. Increasing ionomer content of the CL decreases the relative diffusivity in two ways: by decreasing the pore part of the CL which is the part that gas diffusion happens in, and, by resulting in smaller secondary pores which are the main gas diffusion paths (the larger the diameter the lower the gas diffusion resistance). As a result, increasing the ionomer content of the catalyst decreases the gas diffusivity dramatically.

Effect of temperature on relative diffusivity

Binary diffusion is proportional to the absolute temperature to the power of 1.72 [58] (Eq. (14)), while, the Kn diffusivity is a function of absolute temperature to the power of 0.5 [51] (Eq. (12)),

$$D_{\text{binary}} = 1.13 \times 10^{-9} T^{1.724}/p \tag{14}$$

where p is the gas pressure (atm), and T is the absolute temperature (K).

Therefore, when Knudsen diffusion is in effect, the relative diffusivity should change with temperature. The change magnitude can be obtained by temperature dependency analysis. Assuming Knudsen diffusion mechanism is in effect:

$$D^* = \frac{D_{eff}}{D_{\text{binary}}} = \frac{\left(\frac{1}{D_{Kn}} + \frac{1}{D_{\text{molecular}}}\right)^{-1}}{D_{\text{binary}}} = \frac{\frac{D_{\text{molecular}}}{D_{\text{binary}}}}{\left(1 + \frac{D_{\text{molecular}}}{D_{Kn}}\right)} \tag{15}$$

$$D_{molecular} \gg D_{Kn} \xrightarrow{yields} D^* \propto T^{-1.22} \tag{16}$$

Considering Eq. (15), increasing the temperature from 20 °C to 72 °C should decrease the relative diffusivity ~15% for the case where $D_{\text{molecular}} \cong 15 D_{Kn}$ (which was the case here based on the modeling results) if all pores experience Knudsen diffusion.

The experiment results showed a decreasing trend for relative diffusivity versus temperature almost the same as the model prediction. It should be mentioned that, although the relative diffusivity was decreasing with respect to temperature; the effective diffusivity of CL was increasing, but at a lower rate in comparison to binary diffusion.

Model parametric study for gas diffusion

The catalyst ink composition (including I/C), ink process, and CL production method affect gas diffusivity of CL through changing its structure. To investigate effect of structural parameters on the gas diffusivity, the CL design with I/C = 1.1 was considered as the base line here. To simplify the investigation, its PSD was translated to a bi-modal PSD by volume averaging over primary pores and secondary pores. The geometrical parameters of this design are summarized in Table 2.

Porosity

The first parameter to be studied was porosity keeping I/C and PSD constant. Fig. 7a shows that changing porosity from 0.3 to 0.6 (the baseline porosity was 0.58) decreased overlap angle from 44° to 13°. There was not much void space between carbon particles within agglomerates in CL. As a result, changing porosity will affect mostly the geometry in agglomerate scale, which is related directly to the overlap angle of agglomerates. Higher porosities resulted in larger gaps between agglomerates and smaller overlap angles. Therefore, each agglomerate had more available surface area for ionomer to cover, and consequently the ionomer coverage decreased; more primary pores within agglomerates became accessible to gas and the volume of accessible primary pores increased (Fig. 7a).

There were two resistive mechanisms in series in the way of gas diffusion through CL: molecular resistance and Knudsen resistance. While increasing porosity had a direct effect on molecular mechanism and reduced the molecular resistance (Fig. 7b), it had no effect on Knudsen diffusion resistance. In low porosities both molecular and Knudsen mechanisms were limiting factors for gas diffusion, and increasing porosity clearly increased the diffusivity of CL. However, in porosities >0.45 Knudsen resistance became

Table 2 – Geometry parameters of CL base line for model parametric study.

Parameter	Method	Value
Porosity (%)	Analytical (input)	58
Bi-modal PSD	Volume averaging over N_2 adsorption PSD (input)	14 nm 3.5% 201 nm 96.5%
Overlap angle (°)	Model (result)	19
Percentage of open primary pore volume (i.e. not blocked by ionomer) (%) relative to total primary pore volume	Model (result)	11

[6] Agglomerate size distribution.

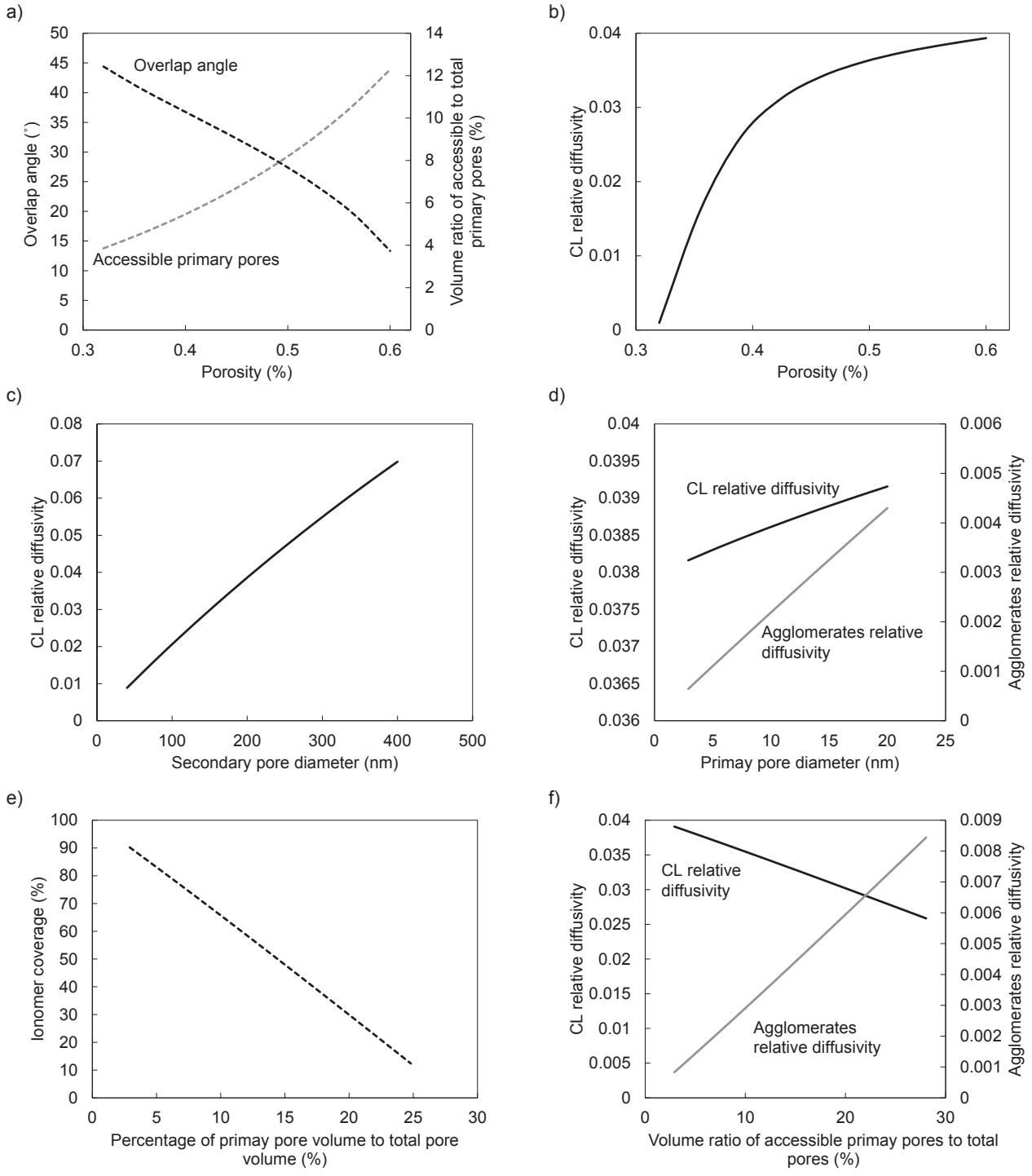

Fig. 7 – a) Modeled overlap angle, and percentage ratio of open primary pores to all primary pores versus porosity of CL. b) Modeled relative diffusivity of CL versus porosity. c) Modeled relative diffusivity of CL versus Secondary pore diameter. d) Modeled relative diffusivity within agglomerates and relative diffusivity of CL versus primary pore diameter. e) Modeled ionomer coverage percentage versus volume percentage of accessible primary pores to all pores. f) Modeled relative diffusivity of CL and relative diffusivity within agglomerates versus volume percentage of accessible primary pores to all pores.

dominant. In this condition changing porosity did not affect CL diffusivity much, and the only way to increase the diffusivity was by decreasing Knudsen resistance (by having larger pores) or increasing the connectivity of pores. This investigation clearly showed the shortcomings of gas diffusion models which consider porosity as the only affecting parameter on the diffusivity.

Secondary pore diameter

Secondary pore diameter affects CL diffusion resistance through Eq. (14). Fig. 7c shows that, the effect of secondary pore diameter is even greater than porosity on relative diffusivity i.e. in the CL the Knudsen diffusion resistance is the dominant resistance.

Primary pore diameter

Primary pore diameter also affects Knudsen diffusion resistance. However, it affects only gas diffusion within agglomerates. Primary pores and secondary pores are two parallel paths with an order of magnitude difference (See the resulted diffusivities in Fig. 7d). Therefore, overall gas diffusivity of CL is mostly function of secondary pores and does not change with size of primary pores. However, gas diffusion within agglomerates is one of the most important processes affecting fuel cell performance, as under operation, oxygen molecules need to reach the reaction sites within the agglomerates. The modeled values for diffusivity within agglomerates were closer to in-situ measured diffusivity values (e.g. 4E-4 at T = 30 °C in Ref. [7]) than ex-situ ones, as, in-situ methods target the gas diffusion that delivers oxygen to reaction site through secondary, then primary pores and ionomer.

Ionomer coverage

To study the effect of ionomer coverage, the measured volume ratio of accessible primary pores in input PSD was manipulated from 3.5% for the real case (almost 90% ionomer coverage) to 25% for the 10% ionomer coverage case (Fig. 7e). More accessible primary pores logically resulted in higher agglomerates relative diffusivity (Fig. 7f). As during this process the actual I/C was kept constant (constant ionomer volume in the unit cell), the ionomer thickness was increasing, filling part of the volume of the secondary pores. Therefore, in this process the overall diffusivity of CL dropped (Fig. 7f). It should be mentioned that ionomer coverage is necessary in fuel cell performance as it is the pathway for ions. As a result, the optimum coverage should be found considering ion conductivity, primary pore accessibility (to provide Pt particles with oxygen), and the overall CL gas diffusivity (to provide the CL with oxygen). Fig. 7e and f provide insight to the relationship between the former two parameters.

Conclusion

A modified Loschmidt cell was used to measure relative diffusivity of three CL designs with I/Cs of 0.5, 1.1, and 1.5 at three different temperatures, 20, 40, and 70 °C. The calculated uncertainty for the measurements was less than 15%. The relative diffusivity of CL with I/C of 0.5 ($D^* = 0.055$) was 80% more than the relative diffusivity of CL with I/C of 1.5 ($D^* = 0.012$). The effective diffusivity of all CLs increased at higher operating temperatures. However, due to Knudsen effect, the rate of increase in effective gas diffusivity of CL was less than the rate for binary diffusion. As a result, the relative diffusivity of CLs (effective diffusivity/binary diffusivity) dropped at 70 °C in comparison with 20 °C operating temperature. The structure of CL was modeled through considering a packed-sphere model for carbon particles within agglomerates, and a network of overlapped spherical agglomerates forming the CL. The gas diffusion problem was solved for the structure considering both molecular and Knudsen mechanisms. The model could predict the relative diffusivities with less than 16% error. Based on both the fundamental diffusion equations and the model, relative diffusivity decreased as operating temperature increased. The parametric study conducted with the model indicated:

- The overall gas diffusivity of CL was mostly dependent on porosity, secondary pore diameters, and the volume percentage of the secondary pores with respect to the total pore volume.
- The Knudsen diffusivity became the dominant limiting factor in high porosities (>0.45) where the sensitivity of diffusivity to porosity decreased.
- Gas diffusivity within agglomerates of CL was linearly dependent on primary pore diameter.
- At constant ionomer content, lowering ionomer coverage increased relative diffusivity within agglomerates and decreased overall diffusivity of CL.

Acknowledgment

This research is supported by funding from the Natural Sciences and Engineering Research Council of Canada (NSERC) Collaborative Research and Development (Grant No. M-CRDPJ453170) and Automotive Fuel Cell Corporation (AFCC). The AFCC Structure, Properties and Performance Research Division is acknowledged for their technical support, and Grant Unsworth from Waterloo Technical Instrument Inc. is acknowledged for performing part of the gas diffusivity tests.

Appendix A. Supplementary data

Supplementary data related to this article can be found at https://doi.org/10.1016/j.ijhydene.2018.07.035.

Appendix B. Model equations derivations

Equation	Explanation
Overlap parameter and unit cell dimension	
$A_{sp} = 4a^2 - a^2(\pi\xi^2 - 4\varphi\xi^2 + 4\tan\varphi) = 4a^2\left(1 + \left(\varphi - \frac{\pi}{4}\right)\xi^2 - \tan\varphi\right)$	(A.1) Cross-sectional area of secondary pores (*sp*) based on cell dimension *a* and overlap parameters (Fig. 3 in the paper)
$r_{sp} = \frac{\sqrt{A_{sp}}}{2} = a\sqrt{1 + \left(\varphi - \frac{\pi}{4}\right)\xi^2 - \tan\varphi}$	(A.2) Relates secondary pore radius to area following Bahrami et al. [59]
$a = \frac{r_{sp}}{\sqrt{1 + (\varphi - \frac{\pi}{4})\xi^2 - \tan\varphi}}$	(A.3) Cell dimension calculation based on secondary pore radius
$r_{agg} = \xi a = \frac{\xi r_{sp}}{\sqrt{1 + (\varphi - \frac{\pi}{4})\xi^2 - \tan\varphi}}$	(A.4) Agglomerate (*agg*) radius calculation based on secondary pore radius
$V_{C-Pt} = V_C + V_{Pt} = V_C + \frac{(V_C\rho_C)\omega_{Pt/C}}{\rho_{Pt}} = V_C\left(1 + \frac{\rho_C\omega_{Pt/C}}{\rho_{Pt}}\right)$	(A.5) Volume of C–Pt particles
$\varepsilon_{C-Pt} = \frac{V_C\varepsilon_C}{V_{C-Pt}} = \varepsilon_C\frac{\rho_{Pt}}{\rho_{Pt} + \rho_C\omega_{Pt/C}}$	(A.5) Porosity of C–Pt particles
$V_{agg} = V_{sphere} - 6V_{cap} = \frac{4\pi a^3}{3}(4.5\xi^2 - 2\xi^3 - 1.5)$	(A.6) Volume of agglomerate, considering Fig. 3 in the paper
$V_I = \frac{(V_C\rho_C)\omega_{I/C}}{\rho_I} = \frac{\rho_{Pt}\rho_C\omega_{I/C}V_{C-Pt}}{\rho_I(\rho_{Pt} + \rho_C\omega_{Pt/C})}$	(A.7) Relates volume of ionomer (I) to C–Pt particles volume
$V_{agg} = V_{C-Pt\ aggr} + V_I = \frac{V_{C-Pt}}{1 - \varepsilon_{FCC}} + \frac{\rho_{Pt}\rho_C\omega_{I/C}V_{C-Pt}}{\rho_I(\rho_{Pt} + \rho_C\omega_{Pt/C})}$	(A.8) Volume of the agglomerate: The summation of volume of C–Pt aggregate (*aggr*) and the ionomer volume surrounding the aggregate
$\varepsilon_{agg} = \frac{\varepsilon_{C-Pt}V_{C-Pt} + V_{C-Pt\ aggr}\varepsilon_{FCC}}{V_{agg}} = \frac{\varepsilon_{C-Pt} + \frac{\varepsilon_{FCC}}{1-\varepsilon_{FCC}}}{\frac{1}{1-\varepsilon_{FCC}} + \frac{\rho_{Pt}\rho_C\omega_{I/C}}{\rho_I(\rho_{Pt} + \rho_C\omega_{Pt/C})}}$	(A.9) The pore volume of agglomerate: The summation of pore volume inside the C–Pt particles and the volume of pore volume around the C–Pt particles (gaps in FCC arrangement)
$\varepsilon_{CL} = 1 - \frac{V_{agg}(1-\varepsilon_{agg})}{8a^3} = 1 - \frac{\pi(1-\varepsilon_{agg})(4.5\xi^2 - 2\xi^3 - 1.5)}{6}$	(A.10) The catalyst layer porosity is the same as unit cell porosity, and the solid parts of the unit cell and agglomerate are the same. This equation is used to calculate the overlap parameter based on CL porosity.
Ionomer coverage	
$V_p = V_{sp} + V_{bpp} + V_{app} = \varepsilon_{CL}V_{unit\ cell} = \varepsilon_{CL}8a^3$	(A.11) *p*: pore, *sp*: secondary pore, *bpp*: blind primary pore, and *app*: accessible primary pore.
$V_{pp} = V_{bpp} + V_{app} = \varepsilon_{agg}V_{agg}$	(A.12) *pp*: primary pore
$\upsilon_{pp/p} = \frac{V_{bpp} + V_{app}}{V_{sp} + V_{bpp} + V_{app}} = \frac{\upsilon_{bpp/app} + 1}{\upsilon_{sp/app} + \upsilon_{bpp/app} + 1}$	(A.13) *υ*: volume ratio. The volume ratio of secondary pores to accessible primary pores (*usp/app*) is known from input PSD, as the input PSD includes only accessible pores.
$\upsilon_{bpp/app} = \frac{\upsilon_{pp/p}(\upsilon_{sp/app} + 1) - 1}{1 - \upsilon_{pp/p}}$	(A.14)
$\upsilon_{pp/p} = \frac{\varepsilon_{agg}V_{agg}}{8a^3\varepsilon_{CL}} = \frac{1-\varepsilon_{CL}}{1-\varepsilon_{agg}} \times \frac{\varepsilon_{agg}}{\varepsilon_{CL}}$	(A.15) Relates the CL and agglomerate porosities to the volume ratio (*υ*) of primary pores to all pores (*pp/p*).
$I_{coverage} = \frac{V_{bpp}}{V_{bpp} + V_{app}} = \frac{\upsilon_{bpp/app}}{\upsilon_{bpp/app} + 1}$	(A.16) The ionomer coverage is defined as ratio of blind primary pores to all primary pores
Gas diffusion	
To solve the diffusion resistance network, the unit cell is divided to two regions (Fig. A1a).	
Region 1: Fig. A1b shows the side view of unit cell and spatial angle θ defined for region one. Considering the up view of the resistance element for region 1 (Fig. A1c) the elemental (*e*) agglomerate radius (r) overlap parameter, overlap angle, and thickness (t) were defined.	
$r_e = \sqrt{r^2 - a^2\tan^2\theta} = a\sqrt{\xi^2 - \tan^2\theta}$	(A.17)
$t_e = ad\ (\tan\theta)$	(A.18)
$\xi_e = \frac{r_e}{a} = \sqrt{\xi^2 - \tan^2\theta}$	(A.19)
$\varphi_e = \cos^{-1}\left(\frac{1}{\xi_e}\right)$	(A.20)
$A_{e\ agg} = 4a^2\left[\left(\frac{\pi}{4} - \varphi_e\right)\xi_e^2 + \tan(\varphi_e)\right]$	(A.21) Area of the agglomerate part of the element
$A_{e\ sp} = 4a^2\left[1 - \tan\varphi_e + \left(\varphi_e - \frac{\pi}{4}\right)\xi_e^2\right]$	(A.21) Area of the secondary pore part of the element
$R_e = \left(\frac{A_{e\ agg}D_{agg}}{t_e} + \frac{A_{e\ sp}D_{sp}}{t_e}\right)^{-1} = \frac{ad(\tan\theta)}{A_{e\ agg}D_{agg} + A_{e\ sp}D_{sp}}$	(A.22) The elemental resistance was calculated considering two parallel resistances for agglomerate and secondary pore parts.
$R_1 = \int_0^{\cos^{-1}\left(\frac{1}{\xi}\right)} \frac{ad(\tan\theta)}{A_{e\ agg}D_{agg} + A_{e\ sp}D_{sp}}$	(A.23)

(continued on next page)

– (continued)

Equation	Explanation
Region 2: Elemental overlap angle become zero in this region, and radius of agglomerate become less than the cell dimension. The angle θ was redefined according to Fig. A1d.	
$r_e = r\cos\theta$	(A.24)
$t_e = rd(\sin\theta) = a\xi d(\sin\theta)$	(A.25)
$A_{e\ agg} = \pi r_e^e = \pi r^2\cos\theta^2 = \pi a^2\xi^2\cos\theta^2$	(A.26)
$A_{e\ sp} = 4a^2 - \pi r^2\cos\theta^2 = a^2(4 - \pi\xi^2\cos\theta^2)$	(A.27)
$R_e = \dfrac{a\xi d(\sin\theta)}{D_{agg}\pi a^2\xi^2\cos\theta^2 + D_{sp}a^2(4 - \pi\xi^2\cos\theta^2)}$	(A.28)
$R_2 = \dfrac{2}{aD_{sp}}\displaystyle\int_{\cos^{-1}\left(\frac{1}{\xi}\right)}^{\frac{\pi}{2} - \cos^{-1}\left(\frac{1}{\xi}\right)} \dfrac{\xi d(\sin\theta)}{4 - \left(1 - \dfrac{D_{agg}}{D_{sp}}\right)\pi\xi^2\cos\theta^2}$	(A.29)
$D_{agg} = (9.09/D_{binary} + 0.18d_{eff\_primary}\sqrt{M/RT})^{-1}$	(A.30) The derivation of agglomerate diffusivity is explained previously.
$D_{sp} = D_{binary}\left(1 + \dfrac{3D_{binary}\sqrt{2\pi M}}{4d_{sp}\sqrt{RT}}\right)^{-1}$	(A.31) The derivation of secondary pore diffusivity is explained previously.
$R_{tot} = R_1 + R_2$	(A.32)
$D^* = \dfrac{1}{2aD_{binary}R_{tot}}$	(A.33)

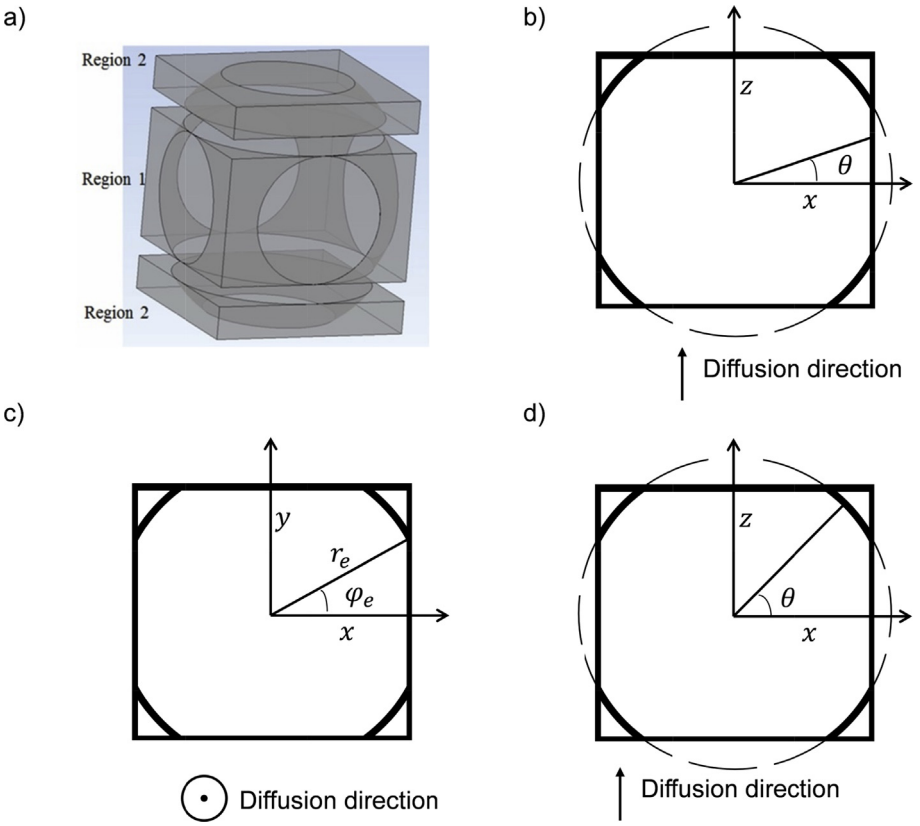

Fig. A1 – a) The unit cell was divided into two regions to solve the gas diffusion resistance problem. b) The side view of the cross-section of the unit cell and considered spacial angle for the first region. c) The top view of the cross-section of the unit cell and considered spacial angle for the second region.

REFERENCES

[1] Mench M. Introduction to fuel cells. Fuel cell engines. Wiley-Blackwell; 2008. https://doi.org/10.1002/9780470209769.ch1.

[2] Inoue G, Kawase M. Effect of porous structure of catalyst layer on effective oxygen diffusion coefficient in polymer electrolyte fuel cell. J Power Sources 2016;327:1–10. https://doi.org/10.1016/j.jpowsour.2016.07.037.

[3] Bruggeman DAG. Berechnung verschiedener physikalischer Konstanten von heterogenen Substanzen. I. Dielektrizitätskonstanten und Leitfähigkeiten der Mischkörper aus isotropen Substanzen. Ann Phys 1935;416:665–79.

[4] Neale GH, Nader WK. Prediction of transport processes within porous media: diffusive flow processes within an homogeneous swarm of spherical particles. AIChE J 2004;19:112–9. https://doi.org/10.1002/aic.690190116.

[5] Eikerling M. Water management in cathode catalyst layers of PEM fuel cells. A structure-based model. J Electrochem Soc 2006;153:E58–70. https://doi.org/10.1149/1.2160435.

[6] Inoue G, Matsukuma Y, Minemoto M. Evaluation of gas diffusion performance in wet GDL with 3D pore network model. ECS Trans 2009;25:1519–27. https://doi.org/10.1017/CBO9781107415324.004.

[7] Wippermann K, Klafki K, Kulikovsky AA. In situ measurement of the oxygen diffusion coefficient in the cathode catalyst layer of a direct methanol fuel cell. Electrochim Acta 2014;141:212–5. https://doi.org/10.1016/j.electacta.2014.06.164.

[8] Kulikovsky AA. A simple equation for in situ measurement of the catalyst layer oxygen diffusivity in PEM fuel cell. J Electroanal Chem 2014;720–721:47–51. https://doi.org/10.1016/j.jelechem.2014.03.005.

[9] Sambandam S, Parrondo J, Ramani V. Estimation of electrode ionomer oxygen permeability and ionomer-phase oxygen transport resistance in polymer electrolyte fuel cells. Phys Chem Chem Phys 2013;15:14994–5002. https://doi.org/10.1039/c3cp51450a.

[10] Liu H, Epting WK, Litster S. Gas transport resistance in polymer electrolyte thin films on oxygen reduction reaction catalysts. Langmuir 2015;31:9853–8. https://doi.org/10.1021/acs.langmuir.5b02487.

[11] Hwang GS, Weber AZ. Effective-diffusivity measurement of partially-saturated fuel-cell gas-diffusion layers. J Electrochem Soc 2012;159:F683–92. https://doi.org/10.1149/2.024211jes.

[12] Baker DR, Caulk D a, Neyerlin KC, Murphy MW. Measurement of oxygen transport resistance in PEM fuel cells by limiting current methods. J Electrochem Soc 2009;156:B991–1003. https://doi.org/10.1149/1.3152226.

[13] He W, Zou J, Wang B, Vilayurganapathy S, Zhou M, Lin X, et al. Gas transport in porous electrodes of solid oxide fuel cells: a review on diffusion and diffusivity measurement. J Power Sources 2013;237:64–73. https://doi.org/10.1016/j.jpowsour.2013.02.089.

[14] Novitski D, Holdcroft S. Determination of O_2 mass transport at the Pt|PFSA ionomer interface under reduced relative humidity. ACS Appl Mater Interfaces 2015;7:27314–23. https://doi.org/10.1021/acsami.5b08720.

[15] Utaka Y, Tasaki Y, Wang S, Ishiji T, Uchikoshi S. Method of measuring oxygen diffusivity in microporous media. Int J Heat Mass Tran 2009;52:3685–92. https://doi.org/10.1016/j.ijheatmasstransfer.2009.02.032.

[16] Flückiger R, Freunberger SA, Kramer D, Wokaun A, Scherer GG, Büchi FN. Anisotropic, effective diffusivity of porous gas diffusion layer materials for PEFC. Electrochim Acta 2008;54:551–9. https://doi.org/10.1016/j.electacta.2008.07.034.

[17] Ismail MS, Ingham DB, Hughes KJ, Ma L, Pourkashanian M. Effective diffusivity of polymer electrolyte fuel cell gas diffusion layers: an overview and numerical study. Int J Hydrogen Energy 2015;40:10994–1010. https://doi.org/10.1016/j.ijhydene.2015.06.073.

[18] Zamel N, Astrath NGC, Li X, Shen J, Zhou J, Astrath FBG, et al. Experimental measurements of effective diffusion coefficient of oxygen-nitrogen mixture in PEM fuel cell diffusion media. Chem Eng Sci 2010;65:931–7. https://doi.org/10.1016/j.ces.2009.09.044.

[19] Rashapov R, Imami F, Gostick JT. A method for measuring in-plane effective diffusivity in thin porous media. Int J Heat Mass Tran 2015;85:367–74. https://doi.org/10.1016/j.ijheatmasstransfer.2015.01.101.

[20] Zhao J, Shahgaldi S, Alaefour I, Yang S, Li X. Pore structure and effective diffusion coefficient of catalyzed electrodes in polymer electrolyte membrane fuel cells. Int J Hydrogen Energy 2018;43:3776–85. https://doi.org/10.1016/j.ijhydene.2018.01.019.

[21] Ostadi H, Rama P, Liu Y, Chen R, Zhang XX, Jiang K. 3D reconstruction of a gas diffusion layer and a microporous layer. J Membr Sci 2010;351:69–74. https://doi.org/10.1016/j.memsci.2010.01.031.

[22] Inoue G, Yokoyama K, Ooyama J, Terao T, Tokunaga T, Kubo N, et al. Theoretical examination of effective oxygen diffusion coefficient and electrical conductivity of polymer electrolyte fuel cell porous components. J Power Sources 2016;327:610–21. https://doi.org/10.1016/j.jpowsour.2016.07.107.

[23] Litster S, Epting WK, Wargo EA, Kalidindi SR, Kumbur EC. Morphological analyses of polymer electrolyte fuel cell electrodes with nano-scale computed tomography imaging. Fuel Cell 2013;13:935–45. https://doi.org/10.1002/fuce.201300008.

[24] Berson A, Choi HW, Pharoah JG. Determination of the effective gas diffusivity of a porous composite medium from the three-dimensional reconstruction of its microstructure. Phys Rev E - Stat Nonlinear Soft Matter Phys 2011;83:1–12. https://doi.org/10.1103/PhysRevE.83.026310.

[25] Siddique NA, Liu F. Process based reconstruction and simulation of a three-dimensional fuel cell catalyst layer. Electrochim Acta 2010;55:5357–66. https://doi.org/10.1016/j.electacta.2010.04.059.

[26] Wu W, Jiang F. Microstructure reconstruction and characterization of PEMFC electrodes. Int J Hydrogen Energy 2014;39:15894–906. https://doi.org/10.1016/j.ijhydene.2014.03.074.

[27] Yu Z, Carter RN. Measurement of effective oxygen diffusivity in electrodes for proton exchange membrane fuel cells. J Power Sources 2010;195:1079–84. https://doi.org/10.1016/j.jpowsour.2009.08.065.

[28] Shen J, Zhou J, Astrath NGC, Navessin T, Liu Z-S, Simon, et al. Measurement of effective gas diffusion coefficients of catalyst layers of PEM fuel cells with a Loschmidt diffusion cell. J Power Sources 2011;196:674–8. https://doi.org/10.1016/j.jpowsour.2010.07.086.

[29] Salari S, McCague C, Tam M, Saha M, Stumper J, Bahrami M. Accurate ex-situ measurements of PEM fuel cells catalyst layer dry diffusivity. ECS Trans 2015;69:419–29.

[30] Radzig AA. Handbook of physical quantities. Boca Raton: CRC Press; 1996.

[31] Rossman RP, Smith WR. Density of carbon black by helium displacement. Ind Eng Chem 1943;35:972–6. https://doi.org/10.1021/ie50405a008.

[32] Zook LA, Leddy J. Density and solubility of nafion: recast, annealed, and commercial films. Anal Chem 1996;68:3793–6. https://doi.org/10.1021/ac960604e.

[33] Salari S, McCague C, Jankovic J, Stumper J, Bahrami M. Structural characterization of PEM fuel cell catalyst layer

using N_2 adsorption porosimetry: effects of ink composition and ink processing. In: Eur. Hydrog. Energy conf. 2018, Malaga; 2018.
[34] De Lange MF, Vlugt TJH, Gascon J, Kapteijn F. Adsorptive characterization of porous solids: error analysis guides the way. Microporous Mesoporous Mater 2014;200:199–215. https://doi.org/10.1016/j.micromeso.2014.08.048.
[35] Wakeham WA, Nagashima A, Sengers JV. Measurement of the transport properties of fluids. Blackwell Scientific Publications; 1991.
[36] Waterloo Technical Instrument. Symmetrical modified Loschmidt cell operator's manual. 2017.
[37] Kinoshita K. Carbon: electrochemical and physicochemical properties. 1988.
[38] Uchida M, Aoyama Y, Eda N, Ohta A. Investigation of the microstructure in the catalyst layer and effects of both perfluorosulfonate ionomer and PTFE-Loaded carbon on the catalyst layer of polymer electrolyte fuel cells. J Electrochem Soc 1995;142:4143–9. https://doi.org/10.1149/1.2048477.
[39] Uchida M. Effects of microstructure of carbon support in the catalyst layer on the performance of polymer-electrolyte fuel cells. J Electrochem Soc 1996;143:2245. https://doi.org/10.1149/1.1836988.
[40] Cheng X, Yi B, Han M, Zhang J, Qiao Y, Yu J. Investigation of platinum utilization and morphology in catalyst layer of polymer electrolyte fuel cells. 1999. p. 75–81.
[41] Kim SH. The effects of catalyst layer microstructure and water saturation on the effective diffusivity in PEMFC 2018;165:468–78. https://doi.org/10.1149/2.0711807jes.
[42] Lavakumar A. Concepts in physical metallurgy. Morgan & Claypool Publishers; 2017. https://doi.org/10.1088/978-1-6817-4473-5.
[43] Ellis A B, Geselbracht MJ, Johnson BJ, Lisensky GC, Robinson WR. Teaching general chemistry: a materials science companion. first ed. American Chemical Society Publication; 1993.
[44] Uchida M, Aoyama Y, Eda N, Ohta A. New preparation method for pPolymer-electrolyte fuel-cells. J Electrochem Soc 1995;142:463–8. https://doi.org/10.1149/1.2044068.
[45] Ihonen J, Jaouen F, Lindbergh G, Lundblad A, Sundholm G. Investigation of mass-transport limitations in the solid polymer fuel cell cathode. J Electrochem Soc 2002;149:A448. https://doi.org/10.1149/1.1456917.
[46] Andreaus B, Eikerling M. Catalyst layer operation in PEM fuel cells: from structural pictures to tractable models. Top Appl Phys 2009;113. https://doi.org/10.1007/978-0-387-78691-9.
[47] Malek K, Eikerling M, Wang Q, Navessin T, Liu Z. Self-organization in catalyst layers of polymer electrolyte fuel cells. J Phys Chem C 2007;111:13627–34. https://doi.org/10.1021/jp072692k.
[48] Cheng B, Ni P, Jin C, Li Z, Zhang D, Dong P, et al. More direct evidence of the fcc arrangement for artificial opal. Optic Commun 1999;170:41–6. https://doi.org/10.1016/S0030-4018(99)00434-4.
[49] Voet A, Aboytes P. Porosity of carbon blacks. Carbon N Y 1971;9:135–8. https://doi.org/10.1016/0008-6223(71)90126-6.
[50] Andisheh-Tadbir M, El Hannach M, Kjeang E, Bahrami M. An analytical relationship for calculating the effective diffusivity of micro-porous layers. Int J Hydrogen Energy 2015;40:10242–50. https://doi.org/10.1016/j.ijhydene.2015.06.067.
[51] Okolo GN, Everson RC, Neomagus HWJP, Roberts MJ, Sakurovs R. Comparing the porosity and surface areas of coal as measured by gas adsorption, mercury intrusion and SAXS techniques. Fuel 2015;141:293–304. https://doi.org/10.1016/j.fuel.2014.10.046.
[52] Pollard WG, Present RD. On gaseous self-diffusion in long capillary tubes. Phys Rev 1948;73:762–74.
[53] Soboleva T, Zhao X, Malek K, Xie Z, Navessin T, Holdcroft S. On the micro-, meso-, and macroporous structures of polymer electrolyte membrane fuel cell catalyst layers. ACS Appl Mater Interfaces 2010;2:375–84. https://doi.org/10.1021/am900600y.
[54] Pant LM, Mitra SK, Secanell M. A generalized mathematical model to study gas transport in PEMFC porous media. Int J Heat Mass Tran 2013;58:70–9. https://doi.org/10.1016/j.ijheatmasstransfer.2012.11.023.
[55] Sobolyeva T. On the microstructure of PEM fuel cell. Simon Fraser University; 2010.
[56] Epting WK, Gelb J, Litster S. Resolving the three-dimensional microstructure of polymer electrolyte fuel cell electrodes using nanometer-scale X-ray computed tomography. Adv Funct Mater 2012;22:555–60. https://doi.org/10.1002/adfm.201101525.
[57] Salari S, Stumper J, Bahrami M. Through plane gas diffusion of catalyst layer of PEMFC: bimodal unit cell modeling. In: 27th inernational symp. Transp. Phenom., Honolulu; 2016.
[58] Marrero TR, Mason EA. Gaseous diffusion coefficients. J Phys Chem Ref Data 1972;1:3.
[59] Bahrami M, Yovanovich MM, Culham JR. Pressure drop of fully-developed, laminar flow in microchannels of arbitrary cross-section. J Fluid Eng 2006;128:1036. https://doi.org/10.1115/1.2234786.